Accepted manuscript doi: 10.1680/jgeot.22.00074

Submitted: 25 February 2022

Published online in 'accepted manuscript' format: 25 January 2023

Manuscript title: Modelling unsaturated silty tailings and the conditions required for static liquefaction

Authors: Yanzhi Wang*, Thanh Vo† and Adrian R. Russell*

Affiliations: *Centre for Infrastructure Engineering and Safety, School of Civil and Environmental Engineering, UNSW Sydney, NSW, Australia and †School of Engineering, The University of Warwick, Coventry, UK

Corresponding author: Adrian R. Russell, Centre for Infrastructure Engineering and Safety, School of Civil and Environmental Engineering, UNSW Sydney, NSW, Australia.

E-mail: a.russell@unsw.edu.au

Accepted manuscript doi: 10.1680/jgeot.22.00074

Abstract

The potential for static liquefaction of tailings is a major focus in the design and operation of tailings storage facilities. This research models the behaviour of unsaturated tailings, with a variety of degrees of saturation, addressing the propensity for static liquefaction during monotonic loading. Unsaturated triaxial tests, including constant suction conditions and constant water-air mass conditions, were performed. A bounding surface plasticity model was used to simulate the results. The constant mass condition is relevant to undrained closed-system loading, which may prevail during fast-deformation after the tailings becomes unstable, when the air and water in the pore space remain locked inside the tailings. Boyle's law and hydraulic hysteresis were accounted for to model the changes of pore air and water pressures, and suction, with the tailings volume change. Good agreements were achieved between test results and model simulations. Additional simulations which mimic rising water tables under constant total stress states in the field, situations which may trigger instabilities, are also shown. Results are added to charts which relate peak and post-liquefaction strengths, and collapse lines, to measures of initial state, for unsaturated conditions, which may be of use in practice.

Keywords: bounding surface model; liquefaction; suction; tailings; unsaturated soil

Accepted manuscript doi: 10.1680/jgeot.22.00074

Introduction

Tailings, being mixtures of water and soil-sized particles, are waste products generated by mining and mineral extraction. Large volumes of tailings are stored on sites, often contained by embankments, forming what are known as tailings storage facilities (TSFs). TSFs fail catastrophically far too often. In many cases the tailings inside a TSF reduces in strength without the addition of significant external disturbances or loads. They may change from a soft/firm solid-like material to a lower strength, almost fluid-like, material (a phenomenon called 'static liquefaction') that can overload the embankment, exit the TSF through a breach and spread many kilometres, destroying lives, property and the environment. Examples of static liquefaction related TSF failures include the 2019 Brumadinho failure (Arroyo & Gens, 2021; Robertson *et al.*, 2021), the 2015 Fundão failure (Sadrekarimi & Riveros, 2020) and the 1994 Merriespruit failure (Fourie *et al*., 2001).

Most studies on static liquefaction have focused on loose and saturated soils and tailings, as loose and fully saturated states are vulnerable to liquefaction in many situations. Correlations have been developed which relate peak and post-liquefaction strengths to measures of initial state, often using the state parameter (ψ) which is the vertical distance between the specific volume (v) and the critical state line in the $v - \ln(p')$ plane, with p' denoting the mean effective stress (Been & Jefferies, 1985; Bobei *et al*., 2009; Mizanur & Lo, 2012). Also, collapse lines (sometimes referred to as instability lines or flow liquefaction lines) in the $q - p'$ plane have been explored, where q denotes the deviatoric stress. The lines represent boundaries between stable and potentially unstable stress states. When above the line a material's behaviour may become unstable, liquefy and flow, if undrained and loose (Ishihara, 1993; Chu & Leong, 2002; Yang, 2002; Lade & Yamamuro, 2011). The correlations and collapse lines are used in stability assessments of TSFs to identify which may be susceptible to static liquefaction-induced failure and require remediation.
Although tailings usually begin their life in a saturated state, desaturation may later occur from exposure to a climate where evapotranspiration exceeds precipitation, irregular deposition patterns of tailings on top of previously dried out surfaces which remain unsaturated as the TSF ages, dewatering, a shifting phreatic surface, or absorption by vegetation.
Unsaturated tailings can also liquefy statically. They can experience a reduction in effective stress and strain soften during closed-system loading, attaining a very low residual strength. The conditions required for it to occur are not well understood although there is evidence of it in poorly graded materials containing predominantly sand sized particles when the degree of saturation (S_{r}) is as low as 90% (Grozic et al., 1999; He & Chu, 2014; Lu *et al.*, 2017; Shi *et al.*, 2021; Świdziński & Smyczyński, 2022). In materials which are well graded, and/or contain significant quantities of silt sized particles, it has occurred when S_{r} is slightly less than 90% (Bella & Musso, 2022). Uzuoka *et al.* (2005) suggested that an unsaturated poorly graded silty fill became fluidized by an earthquake, possibly having an S_{r} as low as 60%, although the supporting data was not strong. When S_{r} is below a certain limit then static

liquefaction will not be possible, although the magnitude of the limit is not well understood. The S_r limit will depend on load path, soil/tailings type and density.

Silty tailings within the shallower portions in several TSFs, to depths of five to ten meters, have been observed to have an S_r ranging from 70% to 100% (Oldecop *et al.*, 2011). Sandy tailings tend to dry out more. One attained S_r ranging from 10% to 40% across the same depth range and under the same climatic conditions as for a silty tailings which attained a S_r of about 80% (Garrino *et al.*, 2017). Particle sizes and grading have an influence on what S_r may be attained, but so does the presence of salt in the pore water (Garino *et al.*, 2022), as would the type and plasticity of any clay minerals present, and layering - especially the thicknesses and extents and whether they comprise predominantly sand, silt or clay sized particles.

Despite many uncertainties there is enough data to suggest that drying may not always result in a S_r that is low enough to prevent the possibility of liquefaction, especially if the tailings are silty and poorly graded. That tailings type is the focus here.

When unsaturated a tailings contains air as well as water in its pore space. A suction (s) is induced, along with suction hardening which is evidenced by an upward s-dependant shift of the critical state line (and isotropic compression line) in the $v - \ln(p')$ plane (Loret & Khalili, 2002). These increase the effective stress of the tailings, cause a strengthening and stiffening and may add to the stability of a TSF pre-liquefaction. Just after an instability commences large deformations may occur quickly. Air will remain trapped in the pore space and its presence makes the tailings compressible, contrary to the fully saturated case where an incompressible (constant volume) condition is maintained during fast deformations. The effective stress alterations, suction hardening, and compressibility must be accounted for when studying static liquefaction of unsaturated materials, identifying the S_r limit and when developing correlations and collapse lines used in stability assessments.

The research on the static liquefaction of unsaturated materials has treated the air and water as one combined compressible fluid (e.g., Mihalache & Buscarnera, 2016; Lü *et al*., 2018), with suction being ignored. Other studies, Unno *et al*. (2008) and Amaratunga & Grozic (2009), treat the air and water phases separately and use Boyle's law to capture volume and pressure changes of the air. Liu & Muraleetharan (2012) coupled compressibility and changes to air and water pressures through capillary plastic moduli rather than adopt Boyle's law. Instability and collapse have been studied by He & Chu (2014) in which the static liquefaction resistance for both triaxial compression and extension were observed experimentally. The strength ratio and the collapse line changed when air was introduced into a sample. In other studies Buscarnera & Nova (2011) and Buscarnera & Prisco (2012) used two approaches, the loss of controllability and the loss of positivity of the second order work, to capture the onset of instability of unsaturated soils under different loading conditions. The two approaches showed agreement between each other. In their theoretical model and experiments, air in the sample was able to drain freely to the atmosphere while water was undrained. This may not be possible in materials with high S_r which deform quickly, limiting the practical applicability of their results.

This research makes further contributions around instability, strength and collapse of an unsaturated silty tailings, giving particular consideration to the presence of air and the way it alters the ability for volume change when it remains trapped inside the tailings. The first part of the research presents an extension of UNSW's bounding surface plasticity model, and uses it to simulate a number of triaxial tests results in which static liquefaction is investigated. A variety of loading conditions, including (i) constant suction and (ii) closed-system (constant mass) loading, are considered. The closed-system loading is particularly relevant to when fast deformations occur after the tailings becomes unstable. In the second part of the research the model is used to explore and simulate how a wider range of initial tailings states and load paths affect the propensity for instability and static liquefaction. Finally, practical implications are demonstrated by adding simulated and measured data, for unsaturated conditions, to charts which relate peak and post-liquefaction strengths, and collapse lines, to measures of initial state. Some charts have been developed for liquefaction induced by cyclic loading (e.g. Zhang *et al.*, 2016), but they are lacking for the static case.

Notations

Conventional triaxial notations are used. $p' = (\sigma_1' + 2\sigma_3')/3$ is the mean effective stress and $q = \sigma_1' - \sigma_3'$ is the deviatoric stress, where σ_1' and σ_3' are the axial and radial effective stresses, respectively. The corresponding strains are $\varepsilon_\mathrm{p} = \varepsilon_1 + 2\varepsilon_3$ and $\varepsilon_\mathrm{q} = \frac{2}{3}(\varepsilon_1 - \varepsilon_3)$, where ε_1 and ε_3 are the axial and radial components. Compressive stress and strains are positive. The incremental form of volumetric strain ε_p is linked to v through:

$$\dot{\varepsilon}_\mathrm{p} = -\frac{\dot{v}}{v} \qquad (1)$$

where $v = 1 + e$ and e is the void ratio. The elastic and plastic strain increments sum to give the total strain increments

$$\begin{bmatrix} \dot{\varepsilon}_\mathrm{p} \\ \dot{\varepsilon}_\mathrm{q} \end{bmatrix} = \begin{bmatrix} \dot{\varepsilon}_\mathrm{p}^\mathrm{e} \\ \dot{\varepsilon}_\mathrm{q}^\mathrm{e} \end{bmatrix} + \begin{bmatrix} \dot{\varepsilon}_\mathrm{p}^\mathrm{p} \\ \dot{\varepsilon}_\mathrm{q}^\mathrm{p} \end{bmatrix} \qquad (2)$$

where the superscripts $^\mathrm{e}$ and $^\mathrm{p}$ denote elastic and plastic components, respectively.

Model

The bounding surface plasticity model employed in this research is that presented by Russell & Khalili (2006). Here, for the first time, adaptations are made for the simulation of closed-system loading conditions, meaning the pore air and pore water in the modelled material remain unvented to the atmosphere. This is of practical relevance when loading, deformation and failure happen quickly, for example when the material becomes unstable and liquefies. Boyle's law captures the pressure and volume of the air phase. There is no need to apply Henry's law to capture the dissolved air as it was found to have negligible influence (less than 1%) on the computed air and water pressures.

Accepted manuscript doi: 10.1680/jgeot.22.00074

3.1 Effective stress

The effective stress concept (Bishop, 1959; Khalili *et al*., 2004) is adopted, where

$$\sigma = \sigma' - \chi s + u_{\mathrm{a}} \qquad (3)$$

in which σ denotes the total stress, σ' denotes the effective stress, $s = u_{\mathrm{a}} - u_{\mathrm{w}}$ is the matric suction, and u_{a} and u_{w} are pore air and water pressures, respectively. Atmospheric pressure (u_{atm}) is taken to be the datum, meaning σ, σ', u_{a} and u_{w} are zero when equal to that pressure. The total stress in excess of u_{a} is referred to as a net stress, denoted using a subscript $_{\mathrm{n}}$, i.e. $\sigma_{\mathrm{n}} = \sigma - u_{\mathrm{a}}$. χs is the contribution of suction to the effective stress. When the material is saturated, $\chi = 1$ and $\sigma = \sigma' + u_{\mathrm{w}}$. When the material is dry $\chi = 0$ and $\sigma = \sigma' + u_{\mathrm{a}}$. When the material is in an unsaturated state the definition for χ from Khalili & Khabbaz (1998) and Khalili & Zargarbashi (2010) is adopted here. When the soil is experiencing main wetting or drying

$$\chi = \begin{cases} 1 \text{ for } \frac{s}{s_{\mathrm{e}}} \leq 1 \\ \left(\frac{s}{s_{\mathrm{e}}}\right)^{-\Omega} \text{ for } \frac{s}{s_{\mathrm{e}}} \geq 1 \end{cases} \qquad (4)$$

where Ω is a material constant with the best fit of 0.55 for a wide variety of soils and tailings, comprising different combinations of sand, silt and clay sized particles. Ω also represents the slope of the relationship between χ and $\frac{s}{s_{\mathrm{e}}}$ in a double logarithmic plane. s_{e} is the air entry (s_{ae}) or air expulsion (s_{ex}) value, depending on whether the sample is experiencing main drying or main wetting. When the hydraulic state is on a scanning curve

$$\chi = \begin{cases} \left(\frac{s_{\mathrm{rd}}}{s_{\mathrm{ae}}}\right)^{-\Omega} \left(\frac{s}{s_{\mathrm{rd}}}\right)^{-\zeta} \text{ for drying path reversal } \left(\frac{s_{\mathrm{ex}}}{s_{\mathrm{ae}}}\right)^{\frac{\Omega}{\Omega-\zeta}} s_{\mathrm{rd}} \leq \mathrm{s} \leq s_{\mathrm{rd}} \\ \left(\frac{s_{\mathrm{rw}}}{s_{\mathrm{ex}}}\right)^{-\Omega} \left(\frac{s}{s_{\mathrm{rw}}}\right)^{-\zeta} \text{ for wetting path reversal } s_{\mathrm{rw}} \leq s \leq \left(\frac{s_{\mathrm{ae}}}{s_{\mathrm{ex}}}\right)^{\frac{\Omega}{\Omega-\zeta}} s_{\mathrm{rw}} \end{cases} \qquad (5)$$

where ζ is another material constant and slope. s_{rd} and s_{rw} denote the suction values where the scanning curve intersects the main drying and wetting curves, respectively.

3.2 Water retention properties

For a given e, s is related to S_{r} through the water retention curve (WRC), which comprises main wetting and drying branches defined using

$$S_{\mathrm{r}} = \begin{cases} 1 \text{ when } s \leq s_{\mathrm{e}} \\ \left(\frac{s}{s_{\mathrm{e}}}\right)^{-\alpha} \text{ when } s \geq s_{\mathrm{e}} \end{cases} \qquad (6)$$

where α is a material constant. For scanning paths S_{r} is linked to s through

$$S_{\mathrm{r}} = \begin{cases} \left(\frac{s_{\mathrm{ae}}}{s_{\mathrm{rd}}}\right)^{\alpha} \left(\frac{s}{s_{\mathrm{rd}}}\right)^{-\beta} \text{ for drying path reversal } \left(\frac{s_{\mathrm{ex}}}{s_{\mathrm{ae}}}\right)^{\frac{\alpha}{\alpha-\beta}} s_{\mathrm{rd}} \leq s \leq s_{\mathrm{rd}} \\ \left(\frac{s_{\mathrm{ex}}}{s_{\mathrm{rw}}}\right)^{\alpha} \left(\frac{s}{s_{\mathrm{rw}}}\right)^{-\beta} \text{ for wetting path reversal } s_{\mathrm{rw}} \leq s \leq \left(\frac{s_{\mathrm{ae}}}{s_{\mathrm{ex}}}\right)^{\frac{\alpha}{\alpha-\beta}} s_{\mathrm{rw}} \end{cases} \qquad (7)$$

where β must be defined as $\beta = \frac{\zeta\alpha}{\Omega}$ to maintain compatibility with the χ definition.

If the material has fractal particle and pore size distributions (Russell & Buzzi, 2012; Russell, 2014), like many soils and tailings including that considered here, the influence of e in the WRC is captured in the definitions of s_{ae} and s_{ex}. In particular, $s_{\mathrm{ae}} = C_1 e^{-D_{\mathrm{s}}}$, where C_1 is a material constant and D_{s} is the fractal dimension of the particle size distribution. Also, $s_{\mathrm{ex}} = C_2 s_{\mathrm{ae}} = C_1 C_2 e^{-D_{\mathrm{s}}}$, where C_2 is a material constant. The influence of e can be removed by normalising s using s_{ae} or s_{ex}. Also, $\alpha = 3 - D_{\mathrm{p}}$, where D_{p} is the fractal dimension of the pore size distribution.

Fig. 1 graphs χ and the WRC in the double logarithmic χ, S_{r} versus s/s_{ae} planes.

3.3 The critical state line and isotropic consolidation line

The critical state line (CSL) in the $q - p'$ plane, for saturated and unsaturated conditions, is taken to be a straight line that passes through the origin with slope m_{cs}. m_{cs} relates to the critical state friction angle ϕ'_{cs} through

$$m_{\mathrm{cs}} = \frac{6\sin(\phi'_{\mathrm{cs}})}{3-\sin(\phi'_{\mathrm{cs}})} \qquad (8)$$

In the $v - \ln(p')$ plane the CSL depends on the suction. It is assumed that the CSL is unique for a certain suction ratio $SR = s/s_{\mathrm{ex}}$, defined as

$$v = \begin{cases} \Gamma(SR) - \lambda(SR)\ln(p') \ \text{ when } SR > 1 \\ \Gamma_{\mathrm{sat}} - \lambda_{\mathrm{sat}}\ln(p') \ \text{ when } SR \le 1 \end{cases} \qquad (9)$$

Γ, that is the intercept of the CSL with $p' = 1$ kPa, and λ, the CSL slope, are functions of SR. When the soil is saturated, $SR \le 1$, and Γ and λ are equal to the constants Γ_{sat} and λ_{sat}.

The isotropic compression line (ICL) is assumed to have the same slope as the CSL for a given SR. The intercept of the ICL with $p' = 1$ kPa is denoted N, with N_{sat} and $N(SR)$ corresponding to saturated and unsaturated states. The horizontal distance between the CSL and ICL is a constant for all SR and is controlled by the material parameter R, representing ratios of p' values where the elastic unload-reload line, of slope κ, is intercepted.

3.4 Elasticity

A standard and simple elastic stress-strain relationship is adopted

$$\begin{bmatrix} \dot{\varepsilon}_{\mathrm{p}}^{\mathrm{e}} \\ \dot{\varepsilon}_{\mathrm{q}}^{\mathrm{e}} \end{bmatrix} = \begin{bmatrix} \frac{1}{K} & 0 \\ 0 & \frac{1}{3G} \end{bmatrix} \begin{bmatrix} \dot{p}' \\ \dot{q} \end{bmatrix} \qquad (10)$$

where K is the bulk modulus

$$K = \frac{vp'}{\kappa} \qquad (11)$$

and G is the shear modulus

$$G = \frac{3(1-2\mu)}{2(1+\mu)}K \qquad (12)$$

in which μ is Poisson's ratio, assumed to be 0.3 throughout this study.

3.5 The loading and bounding surfaces

The bounding plasticity surface concept was first proposed by Dafalias & Popov (1975). The current stress state $\boldsymbol{\sigma}' = (p', q)$ is always located on a loading surface. It moves towards an image point $\bar{\boldsymbol{\sigma}}' = (\bar{p}', \bar{q})$ on the bounding surface as plastic deformation occurs. Here $\boldsymbol{\sigma}'$ and $\bar{\boldsymbol{\sigma}}'$ lie on a straight line radiating from the origin, obeying a radial mapping rule. The bounding surface changes in size as plastic hardening or softening occurs. The distance between the loading surface and bounding surface also influences the rate of the plastic deformation.

The loading surface, f, and bounding surface, F, as defined as (Russell & Khalili, 2006)

$$f(p', q, p'_{\mathrm{c}}) = \left(\frac{q}{m_{\mathrm{cs}} p'}\right)^{N_{\mathrm{f}}} - \frac{\ln\left(\frac{p'_{\mathrm{c}}}{p'}\right)}{\ln(R)} = 0 \quad (13)$$

$$F(\bar{p}', \bar{q}, \bar{p}'_{\mathrm{c}}) = \left(\frac{\bar{q}}{m_{\mathrm{cs}} \bar{p}'}\right)^{N_{\mathrm{f}}} - \frac{\ln\left(\frac{\bar{p}'_{\mathrm{c}}}{\bar{p}'}\right)}{\ln(R)} = 0 \quad (14)$$

p'_{c} and $\bar{p}'_{\mathrm{c}}$ control the sizes of the loading and bounding surfaces, representing intercepts with the p' axis. $\bar{p}'_{\mathrm{c}}$ is also the hardening parameter which evolves with changes to $\varepsilon_{\mathrm{p}}^{\mathrm{p}}$ and SR. The loading and bounding surfaces intercept the CSL in the $q - p'$ plane at p' values of p'_{c}/R and $\bar{p}'_{\mathrm{c}}/R$, respectively. The radial mapping rule leads to

$$\frac{\bar{p}'}{p'} = \frac{\bar{q}}{q} = \frac{\bar{p}'_{\mathrm{c}}}{p'_{\mathrm{c}}} \quad (15)$$

and the unit normal vectors at $\boldsymbol{\sigma}'$ and $\bar{\boldsymbol{\sigma}}'$ on the loading and bounding surfaces are the same, denoted $\mathbf{n}$, expressed by

$$\mathbf{n} = \frac{\frac{\partial F}{\partial \bar{\boldsymbol{\sigma}}}}{\left\|\frac{\partial F}{\partial \bar{\boldsymbol{\sigma}}}\right\|} = \frac{\frac{\partial f}{\partial \boldsymbol{\sigma}}}{\left\|\frac{\partial f}{\partial \boldsymbol{\sigma}}\right\|} = [n_{\mathrm{p}} \quad n_{\mathrm{q}}]^{\mathrm{T}} = \left[\frac{\frac{\partial F}{\partial \bar{p}'}}{\sqrt{\frac{\partial F}{\partial \bar{p}'}^2 + \frac{\partial F}{\partial \bar{q}}^2}} \quad \frac{\frac{\partial F}{\partial \bar{q}}}{\sqrt{\frac{\partial F}{\partial \bar{p}'}^2 + \frac{\partial F}{\partial \bar{q}}^2}}\right]^{\mathrm{T}} = \left[\frac{\frac{\partial f}{\partial p'}}{\sqrt{\frac{\partial f}{\partial p'}^2 + \frac{\partial f}{\partial q}^2}} \quad \frac{\frac{\partial f}{\partial q}}{\sqrt{\frac{\partial f}{\partial p'}^2 + \frac{\partial f}{\partial q}^2}}\right]^{\mathrm{T}}$$

(16)

3.6 Plastic potential

A non-associated flow rule is used. The dilatancy d is defined as

$$d = \frac{\dot{\varepsilon}_{\mathrm{p}}^{\mathrm{p}}}{\dot{\varepsilon}_{\mathrm{q}}^{\mathrm{p}}} = (1 + k_{\mathrm{d}}\psi) m_{\mathrm{cs}} - \eta \quad (17)$$

where k_{d} is a material parameter, $\eta = q/p'$ is a stress ratio and ψ is the state parameter, being the vertical distance between the current v and the v on the CSL.

The unit vector $\mathbf{m}$ controlling the relative magnitudes of plastic strain increments is

$$\mathbf{m} = [m_{\mathrm{p}} \quad m_{\mathrm{q}}]^{\mathrm{T}} = \left[\frac{d}{\sqrt{1+d^2}} \quad \frac{1}{\sqrt{1+d^2}}\right]^{\mathrm{T}} \quad (18)$$

Accepted manuscript doi: 10.1680/jgeot.22.00074

3.7 Hardening law

The hardening modulus h comprises two additive parts, $h = h_{\mathrm{b}} + h_{\mathrm{f}}$. h_{b} relates to $\bar{\boldsymbol{\sigma}}'$ on the bounding surface and h_{f} is an arbitrary modulus defined as a function of the distance between $\boldsymbol{\sigma}'$ and $\bar{\boldsymbol{\sigma}}'$. $h_{\mathrm{f}} = 0$ when $\boldsymbol{\sigma}' = \bar{\boldsymbol{\sigma}}'$. The definitions adopted here are

$$h_{\mathrm{b}} = -\frac{\partial F}{\partial \bar{p}'_{\mathrm{c}}}\left(\frac{\partial \bar{p}'_{\mathrm{c}}}{\partial \varepsilon^{\mathrm{p}}_{\mathrm{p}}} + \frac{\partial \bar{p}'_{\mathrm{c}}}{\partial \gamma(SR)}\frac{\partial \gamma(SR)}{\partial SR}\frac{\dot{SR}}{\dot{\varepsilon}^{\mathrm{p}}_{\mathrm{p}}}\right)\frac{m_{\mathrm{p}}}{\left\|\frac{\partial F}{\partial \bar{\sigma}}\right\|} \qquad (19)$$

$$h_{\mathrm{f}} = k_{\mathrm{m}}\frac{\partial \bar{p}'_{\mathrm{c}}}{\partial \varepsilon^{\mathrm{p}}_{\mathrm{p}}}\frac{p'}{\bar{p}'_{\mathrm{c}}}\frac{(\bar{p}'_{\mathrm{c}} - p'_{\mathrm{c}})}{p'_{\mathrm{c}}} \qquad (20)$$

where k_{m} is a material parameter and may be defined in terms of ψ or some other measure of the state. $\gamma(SR)$ relates $\bar{p}'_{\mathrm{c}}$ on the unsaturated CSL to $\bar{p}'_{\mathrm{c0}}$, where $\bar{p}'_{\mathrm{c0}}$ is a corresponding parameter on the saturated CSL. $\gamma(SR)$ is defined as (Loret & Khalili, 2002)

$$\gamma(SR) = \exp\left[\frac{N(SR) - N_{\mathrm{sat}}}{\lambda(SR) - \kappa} - \frac{\lambda(SR) - \lambda_{\mathrm{sat}}}{\lambda(SR) - \kappa}\ln\left(\bar{p}'_{\mathrm{c0}}\right)\right] \qquad (21)$$

in which

$$\bar{p}'_{\mathrm{c0}} = \exp\left(\frac{N_{\mathrm{sat}} - v - \kappa \ln(p')}{\lambda_{\mathrm{sat}} - \kappa}\right) \qquad (22)$$

3.8 Coupling the air and water phases

Here $v_{\mathrm{w}} = S_{\mathrm{r}} e$ denotes the specific pore water volume (i.e. water volume per volume of solid). An increment of s is related to increments of e and v_{w} (Yang & Russell, 2015)

$$\dot{v}_{\mathrm{w}} = (S_{\mathrm{r}} + \frac{\partial S_{\mathrm{r}}}{\partial e})\dot{e} + \frac{\partial S_{\mathrm{r}}}{\partial s}\dot{s} \qquad (23)$$

where $\frac{\partial S_{\mathrm{r}}}{\partial e}$ and $\frac{\partial S_{\mathrm{r}}}{\partial s}$ are obtained from the WRC equations.

Boyle's law couples the volume and pressure change of the air phase

$$(u_{\mathrm{a}} + u_{\mathrm{atm}})v_{\mathrm{a}} = C \qquad (24)$$

where $u_{\mathrm{a}} + u_{\mathrm{atm}}$ is the absolute pore air pressure and $v_{\mathrm{a}} = (1 - S_{\mathrm{r}})e$ is the specific air volume (i.e. the air volume per volume of solid). C is a constant depending on the initial values of v_{a} and u_{a}. The incremental form becomes

$$(u_{\mathrm{a}} + u_{\mathrm{atm}})\dot{v}_{\mathrm{a}} + \dot{u}_{\mathrm{a}} v_{\mathrm{a}} = 0 \qquad (25)$$

In a closed-system the volume changes of the solid particles and water are sufficiently small compared to the air volume change and can be assumed zero, so that $\dot{v}_{\mathrm{a}} = \dot{v} - \dot{v}_{\mathrm{w}} = \dot{v}$.

Test procedure and model calibration

The model is now fitted to triaxial test results. The tailings, from a gold mine, is a sandy silt with a fines content of 59% and D_{s} = 2.618. It has a specific gravity of $G_{\mathrm{s}} = 2.78$, and a liquid limit and plastic limit of 18% and 16%, respectively (Ayala *et al*., 2020; Vo *et al*., 2022). Saturated triaxial tests were conducted to find the CSL (Reid *et al*., 2021). The unsaturated triaxial test results considered here are for both: (i) constant s shearing and (ii) constant water and air mass (i.e. closed-system) shearing.

4.1 Tests conducted

Filter paper tests and pressure plate tests revealed the WRC, defined by parameters α = 0.65, β = 0.18, C_1 = 12 kPa, C_2 = 0.05 (Vo *et al.*, 2022). Ω = 0.55 is adopted for the χ relationship, meaning ζ = 0.15.

The constant s tests were conducted using a Bishop-Wesley triaxial testing system. Cylindrical samples 50 mm in diameter and 100 mm in height were used, formed by compacting three equal layers under a moisture content of 13%. The compacted e ranged from 0.719 to 0.771. The samples were then moved in to the triaxial system. The pore water pressure, applied at the sample base, and cell pressure, were imposed by passing the laboratory's pressurised air through regulators via air-water interface cylinders. The pore air pressure, applied at the sample top, was imposed by passing the laboratory's pressurised air through a regulator.

A compacted sample was made saturated by flushing water through it from bottom to top. The axis translation technique (Hilf, 1956) was then used to impose the target s, being ≈ 50 kPa or ≈ 150 kPa. A sample was also brought to its desired initial net mean stress before shearing, being one of $p_{\mathrm{n0}} \approx$ 20 kPa, 50 kPa or 100 kPa. The volume change of a sample was traced by taking photos, using two cameras at a perpendicular angle, at regular intervals. The photos were processed after the test and the volume of the sample was determined using the sample's sectional areas projected on to the photographs (Bagherieh *et al.*, 2008).

Closed-system tests were conducted using the same system. Samples were flushed to attain S_{r} values that ranged between 63% and 75%. The u_{a} was set to about 10kPa (above u_{atm}). The u_{w} was not measured as it was negative. Then, the valves connected to the air pressure and water pressure lines were closed and shearing commenced. The air pressure sensor connected to the sample top recorded u_{a} reliably. The volume of air in the line and the ceramic pores between the closed valve and sample top was measured to be 18.4 ml. This will be an important consideration when processing the data and applying Boyle's law. The deformation of the pressure line tubing was negligible.

4.2 Model calibration

The saturated CSL in the $v - \ln(p')$ plane (Reid *et al.*, 2021) was fitted using $\lambda_{\mathrm{sat}} = 0.036$ and $\Gamma_{\mathrm{sat}} = 1.781$. The SR dependence was determined using the constant s and closed-system test results. The critical state points approached at the end of those tests are plotted in Fig. 2, along with the corresponding SR values. The parameters providing a fit to the data are

$$\lambda(SR) = \lambda_{\mathrm{sat}} + 4.5\left(SR^{0.004+\frac{0.015}{SR}} - 1\right) \qquad (26)$$

$$\Gamma(SR) = \Gamma_{\mathrm{sat}} + (\lambda - \lambda_{\mathrm{sat}})\ln(2000) \quad (27)$$

These definitions result in all CSLs passing through the same point at $p' = 2000$ kPa, whatever the value of SR, which is a condition imposed only to ensure they do not cross at the lower p' values relevant here. It was found that $\phi'_{\mathrm{cs}} = 34.5°$ and $m_{\mathrm{cs}} = 1.4$.
The elastic parameter $\kappa = 0.009$ was found to be suitable.

The surface shape parameters N_{f} and R were found by assuming $\overline{p}'_{\mathrm{c}} \approx p'_{\mathrm{c}}$ for the loosest triaxial sample, meaning the initial state lies very near the ICL. The subsequent shape of the stress path in the $q - p'$ plane is then similar to the loading surface. $N_{\mathrm{f}} = 2.3$ and $R = 14$ were determined.
It was also found that $k_{\mathrm{d}} = 4$, by trial and error.

Model simulations compared against test data

Model simulations (continuous and dashed lines) and test results (markers) are plotted in Figs. 3 and 4.

5.1 Constant suction shearing tests

Six tests in total were conducted although results and simulations for only three are presented here (Fig. 3) to maintain brevity. The test identifiers and initial conditions are listed in Table 1. Shearing was imposed by keeping u_{a} and u_{w} constant, increasing axial stress while keeping cell pressure constant, i.e. $\mathrm{d}q/\mathrm{d}p_{\mathrm{n}} = 3$. The sample volume changes which occur cause χ and χs to deviate slightly from their initial values meaning $\mathrm{d}q/\mathrm{d}p' \neq 3$.

5.2 Closed-system shearing tests

Five tests in total were conducted and the results and simulations for each are presented in Fig. 4. The test identifiers and initial conditions are listed in Table 2. Additional information regarding the evolution of S_{r} is also presented in Fig. S1 in the supplementary materials. Shearing was imposed by increasing axial stress while keeping cell pressure constant, i.e. $\mathrm{d}q/\mathrm{d}p = 3$. Changes to u_{a} and u_{w} occur during these tests.
The volume of air in the samples, and its compressibility, was sufficient such that the samples exhibited near drained responses at the start of shearing. The lower the S_{r0}, the closer the stress path slope was to $q/p' = 3$. As shearing proceeded, u_{a} increased and the compressibility of the pore air volume reduced, and the responses became more like those for saturated undrained (constant volume) conditions. Similar behaviours have been observed for sand samples by He & Chu (2014) and Mihalache & Buscarnera (2016), although their stress paths considered did not include effective stresses.
The shear strength attained at large strains is heavily influenced by S_{r0} and stress state. There is also a stress path influence as illustrated in the following section. The strength and influences are important in practical situations where closed-system loading is a concern, e.g., in stability assessments of a TSF when post-liquefaction conditions are being considered, which is a standard feature of many international design protocols for TSFs when liquefaction is a possibility. However, the strength and influences are not well understood and rarely, if ever, are considered. They will be explored in more detail in the next section using model simulations.

Accepted manuscript doi:
10.1680/jgeot.22.00074

Simulation of conditions required for static liquefaction

Simulations in the previous section accounted for air inside the air pressure line of the experimental apparatus. Here that component is excluded as the simulations are intended to relate to field situations.

6.1 Parametric analysis

Fig. 5 shows the influence of S_{r0} for the $\frac{\delta q}{\delta p}=3$ load path, $e_0=0.71$ and $p_0'=50$ kPa.

Values of S_{r0}=1, 0.95, 0.9 and 0.85 were considered, which correspond to $\psi_0=0.0698$, 0.0464, 0.0247 and 0.0046. These initial states are for loose tailings that are paste-like in their consistency. The ψ_0 changes with S_{r0} due to the different SR values and CSL locations. The initial χs were obtained by assuming the hydraulic states were located on the main wetting curve. Volumetric compression occurred during subsequent shearing meaning the hydraulic state moved upwards along the main wetting curve.

Hydraulic states located on the main wetting curve have the greatest potential to become unstable by additional wetting. An instability is unlikely to develop during drying of an initially stable tailings, as the tailings is becoming stronger and less able to liquefy. Wetting of an initially stable tailings, on the other hand, could cause an instability as the tailings is becoming weaker and more able to liquefy. In general, wetting, and the possible instability that may result, are of most practical interest.

In Fig. 5, the S_{r0} = 0.95, 0.9 and 0.85 cases resulted in u_{a} = 40.45 kPa, 30.94 kPa and 9.06 kPa being attained at the critical state. As S_{r0} reduced from unity the initial slopes of the $q-p'$ stress paths approached 3.

The line in the $q{-}p'$ plane that passed through the q_{peak} point and origin increased in slope with decreasing S_{r0}. The amount by which q reduced after passing through its peak became less as S_{r0} decreased. In fact, at an S_{r0} value between 0.9 and 0.85, the behaviour changed to one where q continually increased during shear. Instability and flow failures are usually associated with the ability for q to decrease. An S_{r0} value below a certain limit prevents instability from happening, for this load path.

The limiting value of S_{r0}, below which the behaviour is always one of an increasing q, depends on other initial state variables as well. Fig. 6 shows that a decreasing q post-peak is attainable for a decreasing range of S_{r0} values but requires e_0 to increase. Each of the cases shown corresponds to $\psi_0=0.0698$. For the saturated case $\psi_0=0.0698$ means that the initial state is very close to the ICL. For $S_{\mathrm{r0}}=0.85$ the $\psi_0=0.0698$ means that the initial state is midway between the CSL and ICL. A close inspection of the simulations in Fig. 6 reveals there was a slight q increase at the end of the $S_{\mathrm{r0}}=0.85$ simulation.

Fig. 7 shows further influences of e_0. S_{r0} = 0.85 for each case, so the amount of suction hardening present is roughly the same for each as SR depends mostly on S_{r} and slightly on e. $p_0'=50$ kPa and $u_{\mathrm{a0}}=0$ kPa were adopted. At the critical state u_{a} = 28.22 kPa, 37.27 kPa, 42.76 kPa and 45.96 kPa for e_0=0.73, 0.76, 0.79 and 0.85, respectively. The loosest sample experienced the most volumetric compression, meaning the u_{a} at critical state was largest.

The influence of an initially anisotropic stress state is shown in Fig. 8. A range of initial q/p' ratios were considered, corresponding to a variety of $K_0 = \frac{\sigma_3'}{\sigma_1'}$ values. The stress paths during subsequent shearing terminated at nearly the same point in the $q - p'$ plane, but with different e owing to the different S_r values attained. The amount by which q reduced after attaining a peak was heavily influenced by K_0, becoming more pronounced for smaller K_0 values. A smaller K_0 would correspond to a greater strength reduction in a marginally stable tailings that was to suddenly become unstable.

6.2 Influences of stress paths relevant to practical situations

The influences of the total stress paths are explored here. During shearing in saturated undrained conditions, after a given K_0 was applied during consolidation, the effective stress path is not influenced by the total stress path as long as the principal stresses do not rotate. For example, the same effective stress path is observed for axial compression and lateral extension, or for axial extension and lateral compression. The same is not true for unsaturated conditions. The incomplete saturation causes effective stress paths to depend on total stress paths in samples that commence their shearing at the same K_0 consolidated and unsaturated states.

Also considered is the scenario when the pore water pressure increases and causes a reduction in s and p' while q remains constant. This might be caused by the rise of an underlying phreatic surface, for example, or rainfall infiltration.

Fig. 9 shows the influence of total stress paths for a single e_0 and two $S_{\mathrm{r}0}$ values. $p_0' = 50$ kPa, $K_0 = 0.65$, $u_{\mathrm{a}0} = 0$ kPa and $e_0 = 0.74$ were used. The influence of the total stress path on the effective stress path was very minor for $S_{\mathrm{r}0} = 0.95$ although was significant for $S_{\mathrm{r}0} = 0.9$. For both $S_{\mathrm{r}0} = 0.9$ and $S_{\mathrm{r}0} = 0.95$ the final q attained are almost the same.

Attention is now given to the possibility for the onset of instability, from a theoretical viewpoint, and how that may be influenced by the total stress path. Instability becomes possible when the second-order work becomes negative. For a saturated condition the second-order work is defined as

$$d^2W = \frac{1}{2}\left(\dot{p}\dot{\varepsilon}_\mathrm{p} + \dot{q}\dot{\varepsilon}_\mathrm{q} - \dot{u}_w\dot{\varepsilon}_\mathrm{p}\right) \qquad (28)$$

and for undrained triaxial compressive loading, since $\dot{\varepsilon}_\mathrm{p} = 0$, the moment when $d^2W \leq 0$ first occurs coincides with q_peak for loose samples. In dense samples q continually increases in triaxial compression loading and $d^2W > 0$.

For an unsaturated condition an approximation for the second order work is

$$d^2W = \frac{1}{2}\left(\dot{p}\dot{\varepsilon}_\mathrm{p} + \dot{q}\dot{\varepsilon}_\mathrm{q} - \dot{s}\,\dot{v}_\mathrm{w}/(1+e)\right). \qquad (29)$$

The unsaturated form is from Buscarnera & Prisco (2012) but with the inclusion of the work done to compress the air phase in a closed-system. The approximation stems from the omission of the work done by the air-water interface as it moves through the solid skeleton and of the work done to drive the air/water phase in to/out of the material.

Collapse lines (sometimes referred to as instability lines or flow liquefaction lines) are the lines connecting the points where a "soil structure collapse" commences. Collapse becomes possible when $d^2W \leq 0$ first occurs. For saturated undrained cases this coincides with the q_{peak} point. In unsaturated closed-system cases it is very close to (but not exactly at) the q_{peak} point, since $\dot{p}\dot{\varepsilon}_{\mathrm{p}} \approx \dot{s}\,\dot{v}_{\mathrm{w}}/(1+e) = 0$ when q_{peak} is attained. Fig. 10 shows collapse lines for $K_0 = 0.65$ and 0.55, $\delta q/\delta p = 3$ and -1.5, p_0' =25, 50, 75 and 100 kPa, $\psi_0 = 0.0598$ and S_{r0} = 0.85, 0.90, 0.95 and 1.0. For continuous closed-system shearing the lines are mainly influenced by S_{r0}. The influences of K_0, $\delta q/\delta p$ and p_0' are minor.

In another set of simulations the load paths were changed part way through. An initial stress state was assumed, corresponding to a certain K_0. Then the u_{w} and s change monotonically, while p and q remain constant. Once instability became possible, i.e., $d^2W = 0$, the system was closed and the load path was changed to $\frac{\delta q}{\delta p} = -1.5$, i.e. approximating a constant vertical total stress ($\approx \sigma_1$) and a changing horizontal total stress ($\approx \sigma_3$). This mimics what may happen to tailings inside a TSF. The tailings may experience a reducing stability under static conditions, while there are no changes to total stresses, caused by a reduction in effective stress. Once the reduced p' and increased q/p' attain certain magnitudes an instability becomes possible and the material may fail rapidly while maintaining constant mass. The simulations are shown in Figs. 11 and 12.

Fig. 11 is for the saturated case. Initial conditions include $S_{\mathrm{r0}} = 1$, $p_0' = 25$, 50, 75 and 100 kPa, $\psi_0 = 0.0598$ and $K_0 = 0.546$. One conventional undrained triaxial simulation was also included. Solid markers indicate q_{peak} ($d^2W = 0$).

Fig. 12 shows the unsaturated simulations. Initially q, p, u_{a} and p_{n} were kept constant while v_{w}, v_{a} and v varied causing an increase in S_{r}. For $S_{\mathrm{r0}} = 0.90$ the material became potentially unstable, i.e., $d^2W = 0$, while still unsaturated, and from that instant onwards a closed-system condition was assumed along with $\frac{\delta q}{\delta p} = -1.5$, i.e. approximating a constant vertical total stress ($\approx \sigma_1$) and a changing horizontal total stress ($\approx \sigma_3$) condition. For $S_{\mathrm{r0}} = 0.95$ the material became saturated at (almost) exactly the same instant that $d^2W = 0$ was attained, by coincidence. Then, once $d^2W = 0$ was attained, a conventional saturated undrained simulation was used. It so happens that, during instability, σ_3' decreases, while σ_1' and q also decrease. Since p increases then so does σ_3, which is associated primarily with a large build-up of u_{a}. The changes to s and u_{w} are much smaller (Fig. 12b). Fig. S4 in the supplementary material shows these changes. It is possible, for other cases not shown, that d^2W remains positive when saturated and only turns negative after a period of constant q and reducing p'.

In Fig. 10 the collapse lines are (nearly) unique for a given S_{r0} and K_0 = 0.55 or 0.65, and when shearing is continuous and the system remains closed. Those collapse lines do not apply to these alternate simulations, however, which involve an initially reducing p' under constant q. This is illustrated in Fig. S2 in the supplementary material.

6.3 Strengths as a function of initial state

Notations s_{u} and s_{r} are now used, defined as strengths $q_{\mathrm{peak}}/2$ and $q_{\mathrm{cs}}/2$, respectively. They are not undrained shear strengths in the traditional sense, as an undrained strength applies to a saturated and constant volume condition, which is not the situation here for $S_{\mathrm{r0}} < 1$. The strength s_{sl} is also used and represents $q_{\mathrm{sl}}/2$, where q_{sl} is the deviatoric stress at the so called 'localisation point', i.e. the point where the hook occurs in the $q - p'$ plane and a reducing p' changes to an increasing q (Jefferies & Been, 2019). At the localisation point d^2W changes from a negative to a positive, for saturated undrained conditions.

Fig. 13 shows the simulated quantities s_{u}/p'_0, s_{sl}/p'_0 and s_{r}/p'_0 against ψ_0 for a variety of K_0 and S_{r0}. $p'_0 = 50$ kPa was used for all. Fig. 14 shows the same data but presented as $s_{\mathrm{u}}/p_{\mathrm{n0}}$, $s_{\mathrm{sl}}/p_{\mathrm{n0}}$ and $s_{\mathrm{r}}/p_{\mathrm{n0}}$ against a modified state parameter $\psi_{0,\mathrm{m}}$, obtained by ignoring suction. Fig. 14 does not require knowledge of χs or suction hardening to be applied in practice, as $\psi_{0,\mathrm{m}}$ is defined using p_{n0} and the saturated CSL, i.e. as $\psi_{0,\mathrm{m}} = v_0 - (\Gamma - \lambda_{\mathrm{sat}}\ln(p_{\mathrm{n0}}))$. Experimental data, for which K_0=1, are overlaid as markers. Recall that there was extra air volume in the air pressure line that will cause the experimental responses to differ slightly from these simulated responses, but the differences are generally minor. For a certain ψ_0, or $\psi_{0,\mathrm{m}}$, a higher S_{r0} corresponds to a lower s_{u}/p'_0 and s_{r}/p'_0, or $s_{\mathrm{u}}/p_{\mathrm{n}}$ and $s_{\mathrm{r}}/p_{\mathrm{n}}$. When a sample is dense enough there will not be an instability point before the critical state is reached. The q_{peak} will be the critical state point, and the d^2W remains positive always, meaning $s_{\mathrm{u}} = s_{\mathrm{r}}$.

Also shown are lines from Jefferies & Been (2019), being Norsand simulations of shear localizations and critical state shear strengths for a saturated sandy silt tailings.

Fig. 15 shows the brittleness index, $I_{\mathrm{b}} = (s_{\mathrm{u}} - s_{\mathrm{r}})/s_{\mathrm{u}}$, against (a) $\psi_0/\lambda_{\mathrm{e0}}$ and (b) $\psi_{0,\mathrm{m}}/\lambda_{\mathrm{sat}}$ for K_0 = 1, S_{r0} = 1, 0.85 and 0.65 and $p'_0 = 50$ kPa. λ_{e0} is the slope of unsaturated CSL in the $v - \ln(p')$ plane at the start of shear, noting that λ changes slightly during shear for the unsaturated cases. This type of plot is an extension of those used for saturated cases, after Hird & Hassona (1990). The unsaturated cases showed that I_{b} began to rise above zero sooner than the saturated case as $\psi_0/\lambda_{\mathrm{e0}}$ increased. However, the rate of I_{b} increase with increasing $\psi_0/\lambda_{\mathrm{e0}}$ was greater for the saturated case. In other words, a smaller reduction of the initial ψ (or e) will cause a greater reduction of I_{b} for the saturated case than the unsaturated cases.

Accepted manuscript doi: 10.1680/jgeot.22.00074

Conclusions

This paper explores the behaviour of unsaturated silty tailings and the propensity for instability and static liquefaction. It is assumed that a closed-system condition may prevail when the deformation of an unstable tailings happens quickly, as the pore water and air have insufficient time to drain in to or out of the tailings. Boyle’s law was used to capture the pressure and volume change of the compressible air.

A bounding surface plasticity model was used to simulate the tailings’ behaviour under the closed-system condition. Triaxial tests, for both constant suction and closed-system shearing, were performed and simulated by the model with reasonable accuracy. A series of simulations was then carried out to explore the main factors influencing instability. The onset of an instability, in a saturated or unsaturated condition, is indicated by the peak of the effective stress path in the $q - p'$ plane as that is about where the second order work attains a value of zero. From the simulations, in addition to the initial void ratio or state parameter, the initial degree of saturation has the greatest influence on the ability of the tailings to change from being stable to unstable. The compressibility of air, and the effect of suction on the effective stress and the critical state line, each have important contributions. Other factors, including the total stress path, an initially anisotropic stress state, and the initial mean effective stress, have lesser influences. Collapse line slopes may be defined in terms of the initial degree of saturation, and be applicable to a wide range of load paths and initially anisotropic stress states as long as closed-system loading always prevails. The collapse line is less steep, for a certain initial state, when constant q and reducing p' loading is followed by closed-system loading.

Finally, model simulations were used to provide additional data, for a variety of initial degrees of saturation, to charts which relate peak and post-liquefaction strengths to measures of initial state. Two sets of charts were provided, with and without suction influences captured in the mean stress and state parameter calculations, to simplify uptake in industry when knowledge of suction may be unavailable. Additional laboratory tests, considering a wider range of conditions, to support the simulations would be a welcome extension of this research.

Acknowledgements

This work forms part of TAILLIQ (Tailings Liquefaction), which is an Australian Research Council (ARC) Linkage Project (LP160101561) supported by financial and in-kind contributions from Anglo American, BHP, Freeport-McMoRan, Newmont, Rio Tinto and Teck. The TAILLIQ project is being carried out at The University of New South Wales, The University of South Australia, The University of Western Australia (lead organisation) and The University of Wollongong. We acknowledge the support and contributions of project personnel at each of the supporting organisations. The work also forms part of an ARC Future Fellowship (FT200100820) awarded to the corresponding author and that funding is gratefully acknowledged. Financial support from the China Scholarship Council is also gratefully acknowledged.

List of symbols

C	constant in Boyle's law
C_1	constant relating s_{ae} to e
C_2	constant relating s_{ex} to e
d	dilatancy
D_{p}	fractal dimension of the pore size distribution
D_{s}	fractal dimension of the particle size distribution
d^2W	second order work
e	void ratio
F	bounding surface
f	loading surface
G_{s}	specific gravity
g	plastic potential
H	Henry's law constant
h	hardening modulus
h_{b}	part of hardening modulus related to the bounding surface
h_{f}	arbitrary part of the hardening modulus
I_{b}	brittleness index
K	bulk modulus
k_{d}	material parameter controlling the dilatancy
k_{m}	material parameter controlling arbitrary part of the hardening modulus
K_0	ratio of horizontal to vertical effective stress
$\mathbf{m}$	unit normal vector of plastic potential
m_{cs}	slope of the critical state line in $q - p'$ plane

N specific volume on unsaturated isotropic compression line when $p' = 1$ kPa

N_f parameter controlling the shape of the loading and bounding surface

n unit normal vector of the loading and bounding surface

p mean total stress

p' mean effective stress

$\overline{p}'$ corresponding mean effective stress on the bounding surface

p'_c parameter controlling the size of the loading surface

$\overline{p}'_\mathrm{c}$ parameter controlling the size of the bounding surface

p_n mean net stress

q deviatoric stress

q_peak peak deviatoric stress

$\overline{q}$ corresponding deviatoric stress on the bounding surface

R parameter controlling horizontal distance between the critical state line and the isotropic compression line

s suction

s_ae air entry value

s_e air entry or expulsion value

s_ex air expulsion value

S_r degree of saturation

s_r critical state shear strength

s_rd intercept of a scanning curve with the main drying curve

s_rw intercept of a scanning curve with the main wetting curve

s_{sl} strength at shear stress localisation point

s_u peak undrained shear strength

SR suction ratio

u_a pore air pressure

u_w pore water pressure

v specific volume

v_a specific pore air volume

v_w specific pore water volume

α constant related to slopes of main drying and wetting curves

β constant related to slopes of scanning curves

γ parameter relating $\overline{p}'_\mathrm{c}$ to $\overline{p}'_\mathrm{c0}$

Γ parameter controlling the vertical position of the critical state line

ε_{p} volumetric strain

ε_{q} deviatoric strain

ε_1 axial strain

ε_3 radial strain

ζ constant relating s to χ when on scanning curves

η stress ratio

κ slope of the unloading and reloading line in $v - \ln(p')$ plane

λ slope of a critical state line in $v - \ln(p')$ plane

μ poison's ratio

σ total stress

σ_1 total axial stress

σ' effective stress

$\boldsymbol{\sigma}'$ vector indicating current stress state

$\bar{\boldsymbol{\sigma}}'$ vector indicating the stress state at the image point

σ_1' axial effective stress

σ_3' radial effective stress

ϕ_{cs}' triaxial critical state friction angle

χ effective stress parameter

ψ state parameter

Ω constant relating s to χ when on main drying or wetting curve

References

Amaratunga, A. & Grozic, J. (2009) On the undrained unloading behaviour of gassy sands. *Canadian Geotechnical Journal* 46(11):1267-1276.

Arroyo, M. & Gens, A. (2021) Computational analyses of dam I failure at the Corrego de Feijao mine in Brumadinho, International Centre for Numerical. *Methods in engineering* 561.

Ayala, J., Fourie, A. & Reid, D. (2020) Cone penetration testing on silty tailings using a new small calibration chamber. *Géotechnique Letters* 10(4):492-497.

Bagherieh, A., Habibagahi, G. & Ghahramani, A. (2008) A novel approach to measure the volume change of triaxial soil samples based on image processing. *J. Appl. Sci* 8(13):2387-2395.

Been, K. & Jefferies, M. G. (1985) A state parameter for sands. *Géotechnique* 35(2):99-112.

Bella, G. & Musso, G. (2022) Static liquefaction response of silty tailings in nearly saturated conditions.

Bishop, A. W. (1959) The principle of effective stress. *Teknisk ukeblad* 39:859-863.

Bobei, D. C. B. C., Lo, S. R. L. R., Wanatowski, D. W., Gnanendran, C. T. G. T. & Rahman, M. M. R. M. (2009) Modified state parameter for characterizing static liquefaction of sand with fines. *Canadian Geotechnical Journal* 46(3):281-295.

Buscarnera, G. & Nova, R. (2011) Modelling instabilities in triaxial testing on unsaturated soil specimens. *International Journal for Numerical and Analytical Methods in Geomechanics* 35(2):179-200.

Buscarnera, G. & Prisco, C. D. (2012) Discussing the definition of the second-order work for unsaturated soils. *International Journal for Numerical and Analytical Methods in Geomechanics* 36(1):36-49.

Chu, J. & Leong, W. (2002) Effect of fines on instability behaviour of loose sand. *Géotechnique* 52(10):751-755.

Dafalias, Y. & Popov, E. (1975) A model of nonlinearly hardening materials for complex loading. *Acta mechanica* 21(3):173-192.

Fourie, A., Blight, G. & Papageorgiou, G. (2001) Static liquefaction as a possible explanation for the Merriespruit tailings dam failure. *Canadian Geotechnical Journal* 38(4):707-719.

Garino Libardi, L. M., Oldecop, L. A., Romero Morales, E. E. & Rodriguez Pacheco, R. L. (2022) Tailings desiccation process studied in environmental chamber experiment. *Proceedings of the Institution of Civil Engineers-Geotechnical Engineering* 175(2):261-271.

Garino, L. M., Rodari, G. J. & Oldecop, L. A. (2017) Characterization of mine waste materials after 50 years of climate interaction. In *PanAm Unsaturated Soils 2017*.), pp. 270-279.

Grozic, J. L. H. (1999) The behavior of loose gassy sand and its susceptibility to liquefaction.

He, J. & Chu, J. (2014) Undrained responses of microbially desaturated sand under monotonic loading. *Journal of Geotechnical and Geoenvironmental Engineering* 140(5):04014003.

Hilf, J. W. (1956) *An investigation of pore-water pressure in compacted cohesive soils.* University of Colorado at Boulder.

Hird, C. & Hassona, F. (1990) Some factors affecting the liquefaction and flow of saturated sands in laboratory tests. *Engineering Geology* 28(1-2):149-170.

Ishihara, K. (1993) Liquefaction and flow failure during earthquakes. *Géotechnique* 43(3):351-451.

Jefferies, M. & Been, K. (2019) *Soil liquefaction: a critical state approach.* CRC press.

Accepted manuscript doi: 10.1680/jgeot.22.00074

Khalili, N., Geiser, F. & Blight, G. (2004) Effective stress in unsaturated soils: Review with new evidence. *International Journal of Geomechanics* 4(2):115-126.

Khalili, N. & Khabbaz, M. (1998) A unique relationship for χ for the determination of the shear strength of unsaturated soils. *Géotechnique* 48(5):681-687.

Khalili, N. & Zargarbashi, S. (2010) Influence of hydraulic hysteresis on effective stress in unsaturated soils. *Géotechnique* 60(9):729-734.

Lade, P. V. & Yamamuro, J. A. (2011) Evaluation of static liquefaction potential of silty sand slopes. *Canadian Geotechnical Journal* 48(2):247-264.

Liu, C. & Muraleetharan, K. K. (2012) Numerical study on effects of initial state on liquefaction of unsaturated soils. In *GeoCongress 2012: State of the art and practice in geotechnical engineering*.), pp. 2432-2441.

Loret, B. & Khalili, N. (2002) An effective stress elastic–plastic model for unsaturated porous media. *Mechanics of Materials* 34(2):97-116.

Lü, X., Huang, M. & Andrade, J. E. (2018) Modeling the static liquefaction of unsaturated sand containing gas bubbles. *Soils and Foundations* 58(1):122-133.

Lu, X., Huang, M. & Qian, J. (2017) Model Prediction of Static Liquefaction in Unsaturated Sands. In *International Workshop on Bifurcation and Degradation in Geomaterials*.) Springer, pp. 111-116.

Mihalache, C. & Buscarnera, G. (2016) Controllability criteria for soils saturated by a compressible fluid. *Journal of Engineering Mechanics* 142(10):04016076.

Mizanur, R. M. & Lo, S. R. (2012) Predicting the Onset of Static Liquefaction of Loose Sand with Fines. *Journal of Geotechnical and Geoenvironmental Engineering* 138(8):1037-1041.

Oldecop, L., Garino, L., Muñoz, J., Rodríguez, R. & García, C. (2011) Unsaturated behaviour of mine tailings in low precipitation areas. *Unsaturated soils, Taylor & Francis Group, London*:1425-1430.

Reid, D., Fourie, A., Ayala, J. L., Dickinson, S., Ochoa-Cornejo, F., Fanni, R., Garfias, J., Da Fonseca, A. V., Ghafghazi, M. & Ovalle, C. (2021) Results of a critical state line testing round robin programme. *Géotechnique* 71(7):616-630.

Robertson, P. K., De Melo, L., Williams, D. & Wilson, G. W. (2019) Report of the expert panel on the technical causes of the failure of Feijão Dam I. *Commissioned by Vale*.

Russell, A. (2014) How water retention in fractal soils depends on particle and pore sizes, shapes, volumes and surface areas. *Géotechnique* 64(5):379-390.

Russell, A. & Khalili, N. (2006) A unified bounding surface plasticity model for unsaturated soils. *International Journal for Numerical and Analytical Methods in Geomechanics* 30(3):181-212.

Russell, A. R. & Buzzi, O. (2012) A fractal basis for soil-water characteristics curves with hydraulic hysteresis. *Géotechnique* 62(3):269-274.

Sadrekarimi, A. & Riveros, G. A. (2020) Static Liquefaction Analysis of the Fundão Dam Failure. *Geotechnical and Geological Engineering* 38(6):6431-6446.

Shi, Z., Tong, S. & Huang, M. (2021) Evaluation of instability of quasi-saturated sand with entrapped gas due to decreasing total confining stress. *Engineering Geology* 293:106296.

Świdziński, W. & Smyczyński, M. (2022) Modelling of Static Liquefaction of Partially Saturated Non-Cohesive Soils. *Applied Sciences* 12(4):2076.

Unno, T., Kazama, M., Uzuoka, R. & Sento, N. (2008) Liquefaction of unsaturated sand considering the pore air pressure and volume compressibility of the soil particle skeleton. *Soils and Foundations* 48(1):87-99.

Uzuoka, R., Sento, N., Kazama, M. & Unno, T. (2005) Landslides during the earthquakes on May 26 and July 26, 2003 in Miyagi, Japan. *Soils and Foundations* 45(4):149-163.

Vo, T., Wang, Y. & Russell, A. R. (2022) The fall cone test in unsaturated soil and tailings pastes. *Géotechnique* 72(3):274-281.

Yang, H. & Russell, A. R. (2015) Cavity expansion in unsaturated soils exhibiting hydraulic hysteresis considering three drainage conditions. *International Journal for Numerical and Analytical Methods in Geomechanics* 39(18):1975-2016.

Yang, J. (2002) Non-uniqueness of flow liquefaction line for loose sand. *Géotechnique* 52(10):757-760.

Zhang, B., Muraleetharan, K. K. & Liu, C. (2016) Liquefaction of unsaturated sands. *International Journal of Geomechanics* 16(6):D4015002.

Table 1. Initial conditions of the constant suction triaxial shear tests

Test ID.	p_{n0} (kPa)	s (kPa)	S_{r0}	e_0	χ	χs (kPa)
14	19.3	50.8	0.37	0.74	0.57	29.2
17	98.1	51.8	0.39	0.75	0.57	29.5
18	48.0	150.2	0.23	0.72	0.40	60.2

Table 2. Initial conditions of closed-system triaxial shearing tests

Test ID.	p_{n0} (kPa)	s (kPa)	S_{r0}	e_0	χ	χs (kPa)
2	12.9	1.46	0.68	0.90	0.72	1.03
3	28.9	1.50	0.67	0.89	0.71	1.07
4	45.5	1.56	0.65	0.89	0.70	1.09
5	15.0	1.25	0.75	0.89	0.79	0.99
6	32.3	1.42	0.63	0.94	0.68	0.97

Figure captions

Fig. 1. S_{r} and χ plotted against s/s_{ae} in double logarithmic planes

Fig. 2. Critical state points from test data under different SR, plotted together with the fitted CSLs. The $SR \approx 1.6$ group was from the closed-system test results. The $SR \approx 48$ and $SR \approx 145$ groups were from constant s test results. The numbers beside the markers and lines show the SR value of the corresponding test and fitted result at the critical state

Fig. 3. Constant suction triaxial shearing test results and simulations for Test 14 ($s = 50.84$ kPa, $p_{\mathrm{n0}} = 19.26$ kPa, $e_0 = 0.74$), Test 17 ($s = 51.82$ kPa, $p_{\mathrm{n0}} = 98.11$ kPa, $e_0 = 0.75$) and Test 18 ($s = 150.18$ kPa, $p_{\mathrm{n0}} = 48.04$ kPa, $e_0 = 0.72$)

Fig. 4. Closed-system test results and simulations for the initial conditions of Test 2 ($S_{\mathrm{r0}} = 0.68$, $p_{\mathrm{n0}} = 12.86$ kPa, $e_0 = 0.90$), Test 3 ($S_{\mathrm{r0}} = 0.67$, $p_{\mathrm{n0}} = 28.79$ kPa, $e_0 = 0.89$), Test 4 ($S_{\mathrm{r0}} = 0.65$, $p_{\mathrm{n0}} = 45.45$ kPa, $e_0 = 0.89$), Test 5 ($S_{\mathrm{r0}} = 0.75$, $p_{\mathrm{n0}} = 15.00$ kPa, $e_0 = 0.89$) and Test 6 ($S_{\mathrm{r0}} = 0.63$, $p_{\mathrm{n0}} = 32.30$ kPa, $e_0 = 0.94$)

Fig. 5. Simulation of closed-system shearing for S_{r0} =1, 0.95, 0.9 and 0.85, with $e_0 = 0.71$, $p'_0 = 50$ kPa, $q_0 \approx 0$ and $\delta q/\delta p = 3$. The first number inside the parentheses represents S_{r0}, the second represents ψ_0. Markers represent q_{peak} points

Fig. 6. Simulation results of closed-system shearing for S_{r0} =1, 0.95, 0.9 and 0.85, $p'_0 = 50$ kPa, $q_0 \approx 0$, $\delta q/\delta p = 3$ and $\psi_0 = 0.0698$. The first number in each parentheses represents S_{r0}, the second represents e_0. Markers represent q_{peak} points

Fig. 7. Simulation of closed-system shearing for $S_{\mathrm{r0}} = 0.85$, e_0 =0.82, 0.79, 0.76 and 0.73, $p'_0 = 50$ kPa, $q_0 \approx 0$ and $\delta q/\delta p = 3$. Numbers in the parentheses represent e_0. Markers represent q_{peak} points

Fig. 8. Simulation of closed-system shearing for $p'_0 = 50$ kPa, $\delta q/\delta p = 3$, $e_0 = 0.75$, $S_{\mathrm{r0}} = 0.9$ and $K_0 \approx 1$, 0.85, 0.65, 0.55 and 0.45. Numbers in the parentheses represent K_0. Markers represent q_{peak} points

Accepted manuscript doi: 10.1680/jgeot.22.00074

Fig. 9. Simulations of closed-system shearing. $e_0 = 0.74$, $p'_0 = 50$ kPa, $S_{\mathrm{r0}} = 0.95$ and 0.9, total stress path $\delta q/\delta p$ ranges from -3 to 3, and $K_0 = 0.65$. The first number in each parentheses represents the S_{r0}. The numbers after the first comma represent $\delta q/\delta p$. Directions of arrows crossing the simulations show the change of $\delta q/\delta p$ and correspond to the → arrows in the parentheses. Arrows with dashed lines in Fig. 9(a) illustrate the directions of the total stress paths. In a clockwise direction they represent $\frac{\delta q}{\delta p} = -1.5, -2, -3,$ 0 and 3. Markers represent q_{peak} points

Fig. 10. Simulation of continuous closed-system shearing, with markers representing q_{peak} (d^2W ≈0). $S_{\mathrm{r0}} = 0.85$, 0.9, 0.95 and 1.0, $K_0 = 0.65$ and 0.55, $\frac{\delta q}{\delta p} = 3$ and $-$ 1.5 and p'_0 =25, 50, 75 and 100 kPa and $\psi_0 = 0.0598$ were used. Numbers in the parentheses represent S_{r0}.

Fig. 11. Simulation of static liquefaction due to water intrusion. $S_{\mathrm{r}} = 1$, $\psi_0 = 0.0598$, $K_0 = 0.546$ and p'_0 =25, 50, 75 and 100 kPa were used

Fig. 12. Simulation of unsaturated static liquefaction. q and p remain constant during water intrusion until an instability develops, after which a closed-system $\mathrm{d}q/\mathrm{d}p = -1.5$ load path applies. Initial conditions include $e_0 = 0.81$, $p'_0 = 50$ kPa, S_{r0} =0.95 and 0.90, and $K_0 = 0.5$. Initial hydraulic states were assumed to be on the top scanning curve of the WRC. Markers represent q_{peak} (d^2W ≈0). Numbers in the parentheses represent S_{r0}

Fig. 13. Summary of simulation data and closed-system test data plotted in the s_{u}/p'_0 , s_{sl}/p'_0 and s_{r}/p'_0 versus ψ_0 planes. Solid and hollow markers represent s_{u}/p'_0 and s_{r}/p'_0 from the closed-system tests, respectively. Numbers beside the markers indicate S_{r0}. The first number in the legend represents S_{r0}, and the second represents K_0 in (a), and residual (r) or localisation (sl) strength in (b). *typical relationships for saturated sandy silt tailings, taken from Jefferies & Been (2019), are shown in (b) using grey lines

Fig. 14. Summary of simulation data and closed-system test data plotted in the $s_{\mathrm{u}}/p_{\mathrm{n0}}$, $s_{\mathrm{sl}}/p_{\mathrm{n0}}$ and $s_{\mathrm{r}}/p_{\mathrm{n0}}$ versus $\psi_{0,\mathrm{m}}$ planes. Solid and hollow markers represent $s_{\mathrm{u}}/p_{\mathrm{n0}}$ and $s_{\mathrm{r}}/p_{\mathrm{n0}}$ from the closed-system tests, respectively. Numbers beside the markers indicate S_{r0}. The first number in the legend represents S_{r0}, and the second represents K_0 in (a), and residual (r) or localisation (sl) strength in (b). *typical relationships for a saturated sandy silt tailings, taken from Jefferies & Been (2019), are shown in (b) using grey lines

Fig. 15. Summary of simulation data and closed-system test data plotted in the I_{b} versus (a) $\psi_0/\lambda_{\mathrm{e0}}$ and (b) $\psi_{0,\mathrm{m}}/\lambda_{\mathrm{sat}}$ planes. Markers represent data from the closed-system tests. Numbers beside the solid markers indicate S_{r0}. *typical relationships for saturated sands including mines and oil sands tailings, taken from Jefferies & Been (2019), are shown

Accepted manuscript doi:
10.1680/jgeot.22.00074

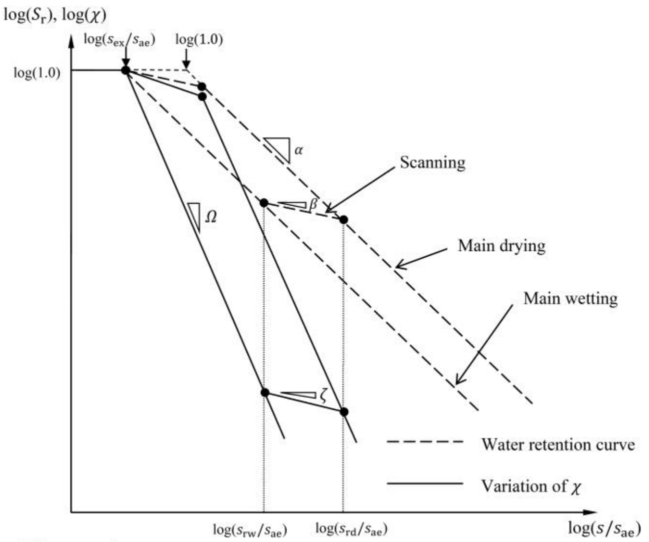

Figure 1

Accepted manuscript doi:
10.1680/jgeot.22.00074

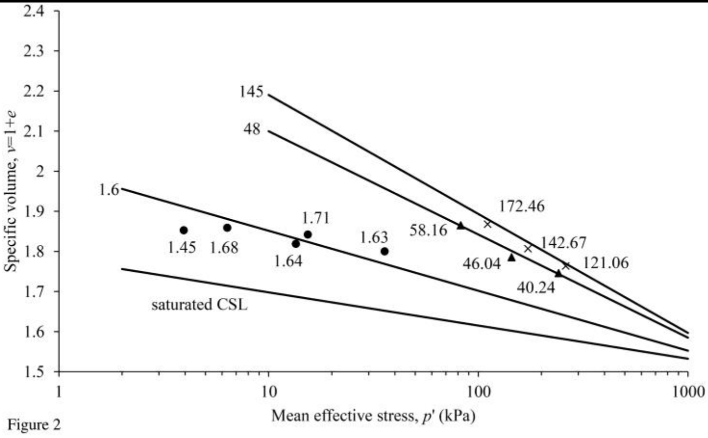

Figure 2

Accepted manuscript doi: 10.1680/jgeot.22.00074

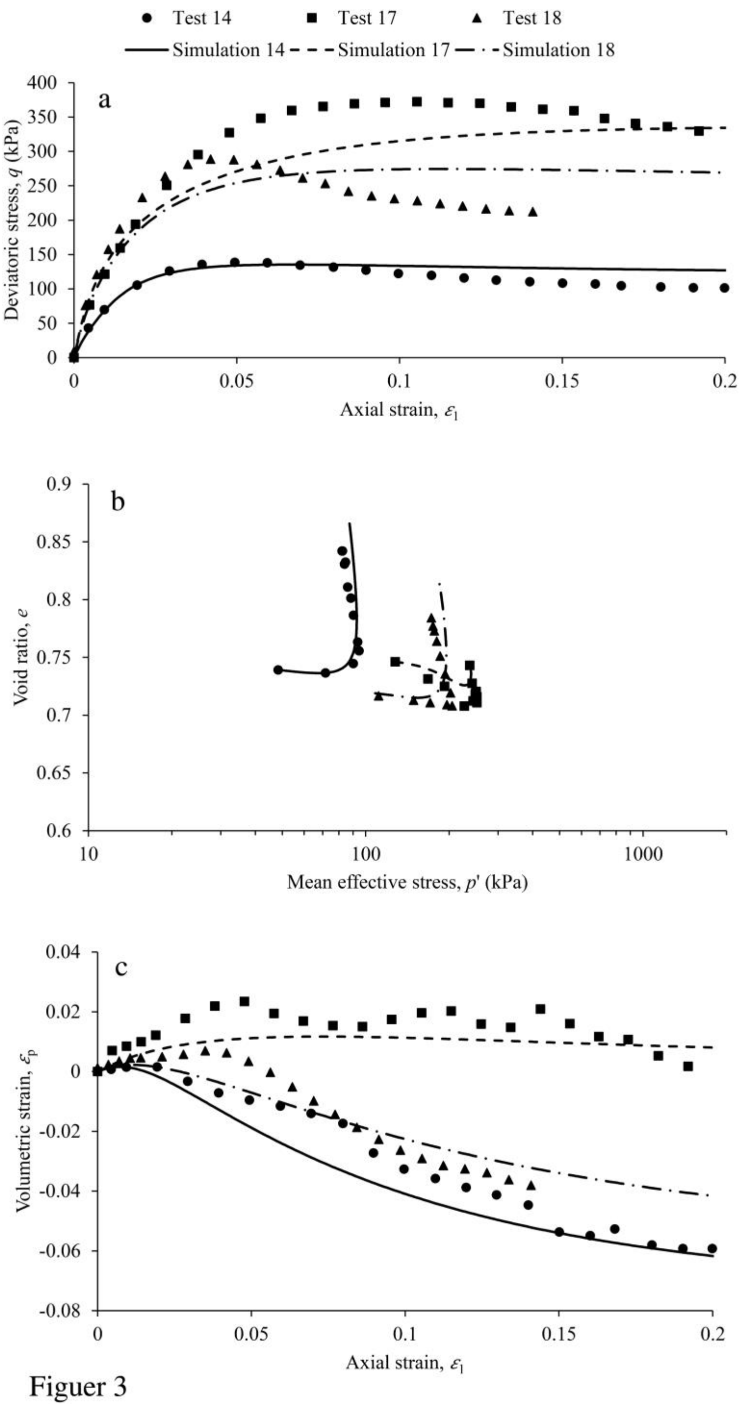

Figuer 3

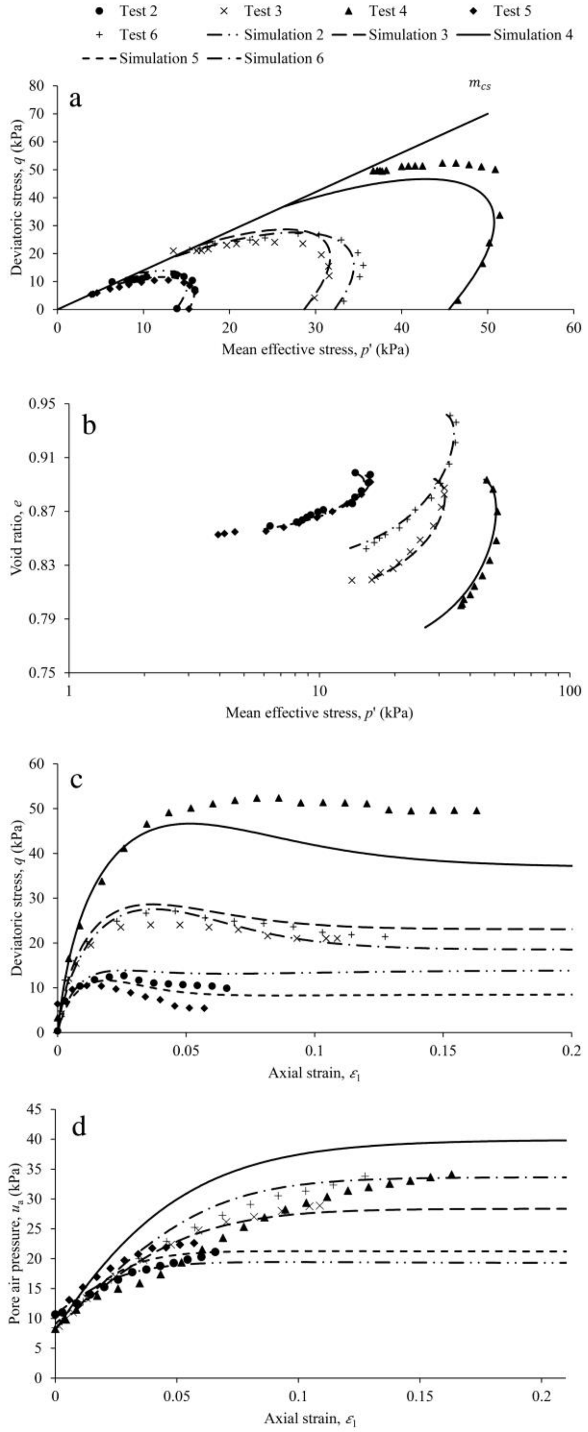
Test 2
Test 3
Test 4
Test 5
Test 6
Simulation 2
Simulation 3
Simulation 4
Simulation 5
Simulation 6
a
m_{cs}
Deviatoric stress, q (kPa)
Mean effective stress, p' (kPa)
b
Void ratio, e
Mean effective stress, p' (kPa)
c
Deviatoric stress, q (kPa)
Axial strain, ε_1
d
Pore air pressure, u_a (kPa)
Axial strain, ε_1

Figure 4

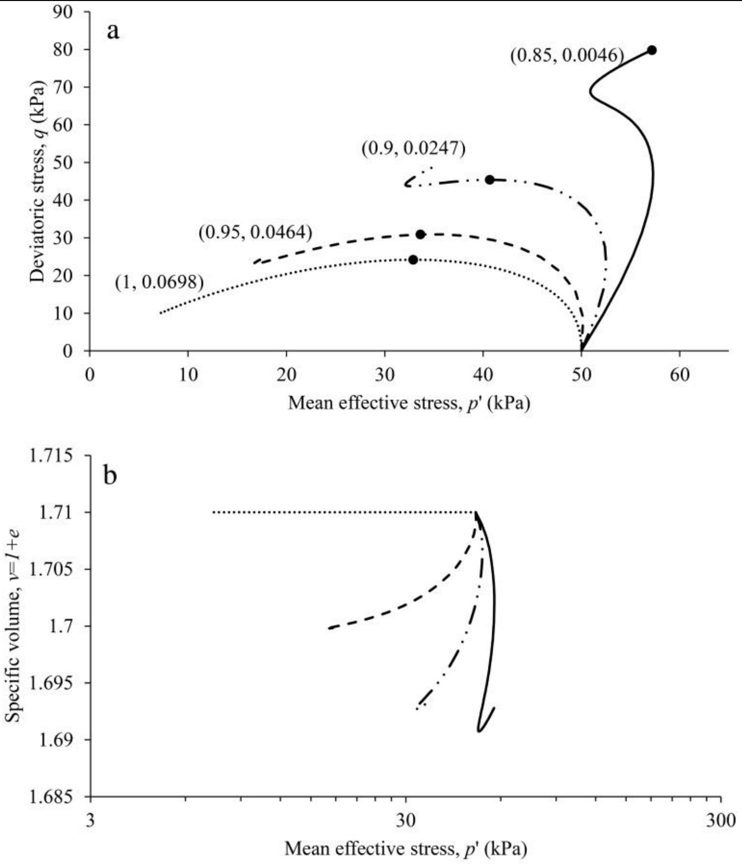
a
(0.85, 0.0046)
(0.9, 0.0247)
(0.95, 0.0464)
(1, 0.0698)
Deviatoric stress, q (kPa)
Mean effective stress, p' (kPa)
b
Specific volume, v=1+e
Mean effective stress, p' (kPa)

Figure 5

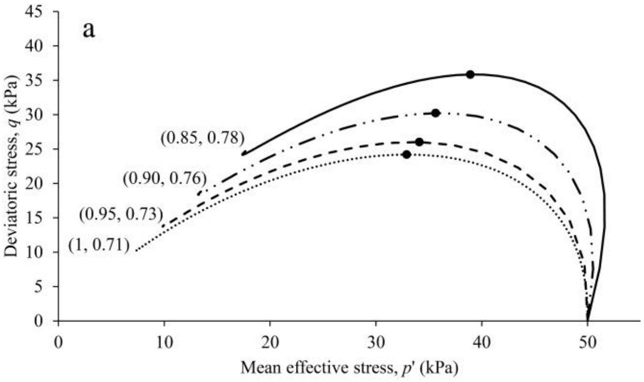
a
Deviatoric stress, q (kPa)
Mean effective stress, p' (kPa)
(0.85, 0.78)
(0.90, 0.76)
(0.95, 0.73)
(1, 0.71)
0
5
10
15
20
25
30
35
40
45
0
10
20
30
40
50

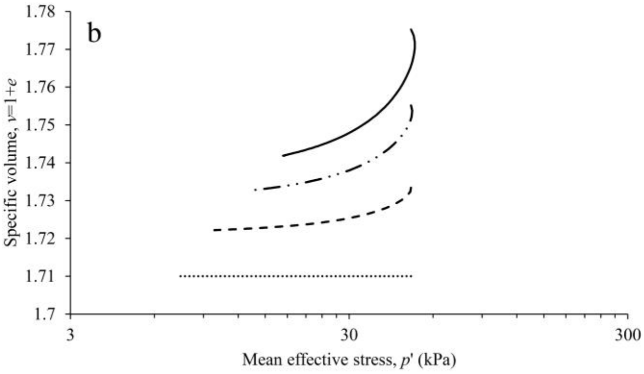
b
Specific volume, v=1+e
Mean effective stress, p' (kPa)
1.7
1.71
1.72
1.73
1.74
1.75
1.76
1.77
1.78
3
30
300

Figure 6

Accepted manuscript doi: 10.1680/jgeot.22.00074

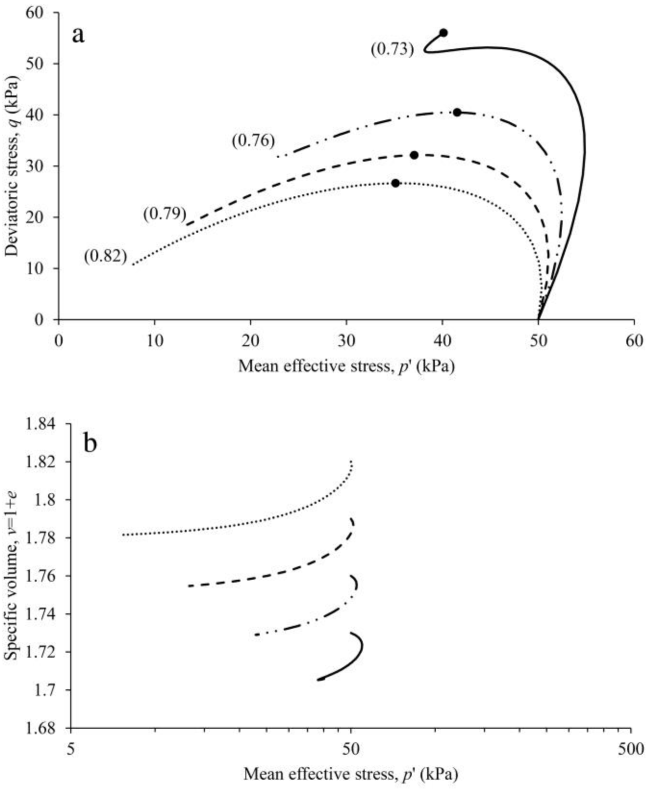

Figure 7

Accepted manuscript doi:
10.1680/jgeot.22.00074

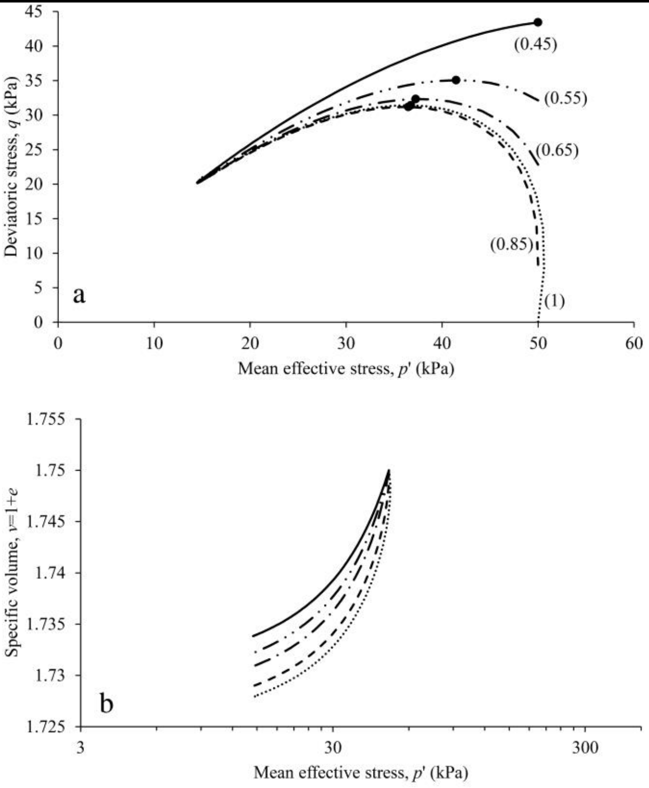

Figure 8

Accepted manuscript doi:
10.1680/jgeot.22.00074

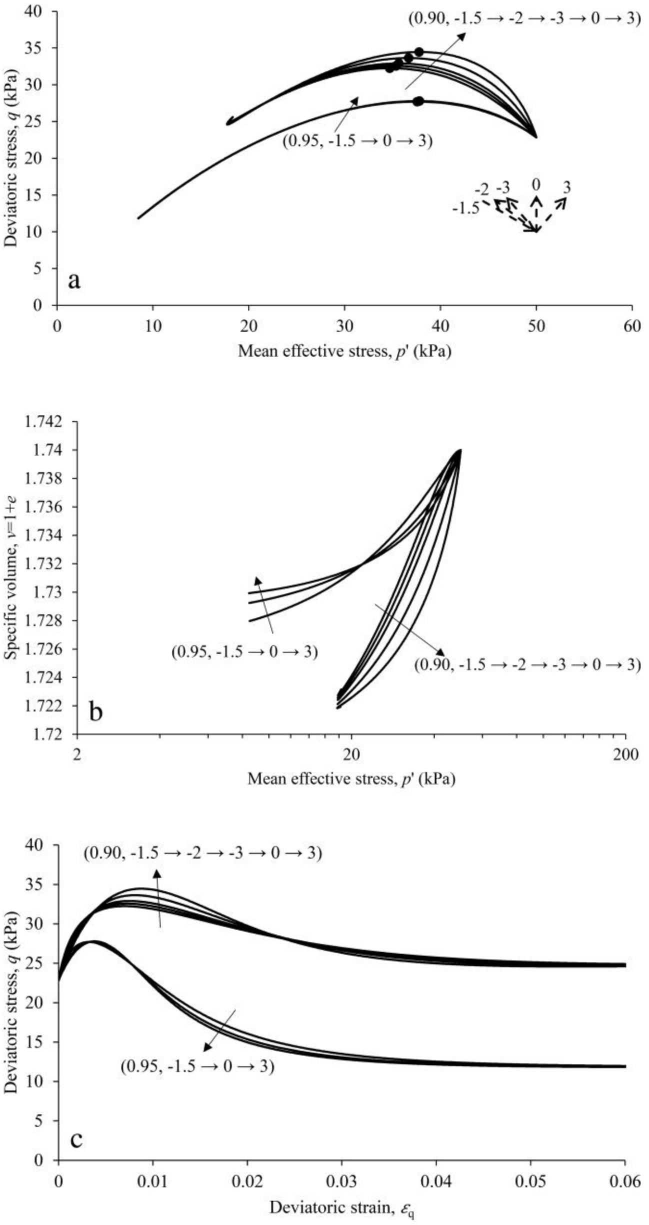

Figure 9

Accepted manuscript doi: 10.1680/jgeot.22.00074

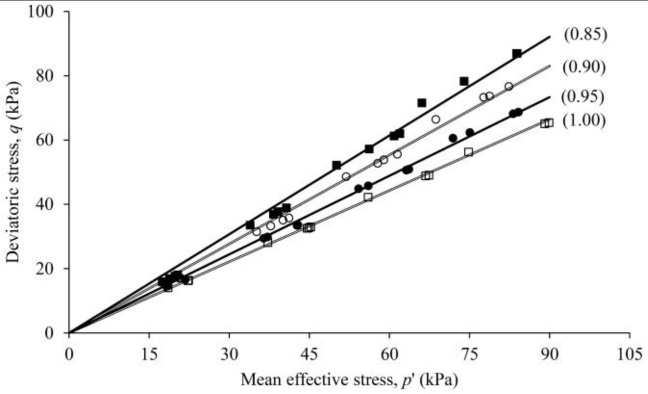

Figure 10

Accepted manuscript doi:
10.1680/jgeot.22.00074

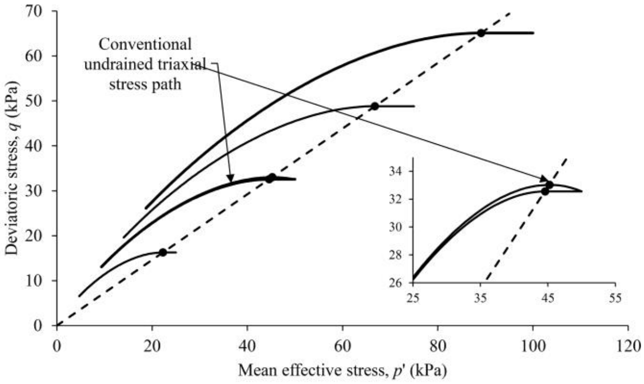

Figure 11

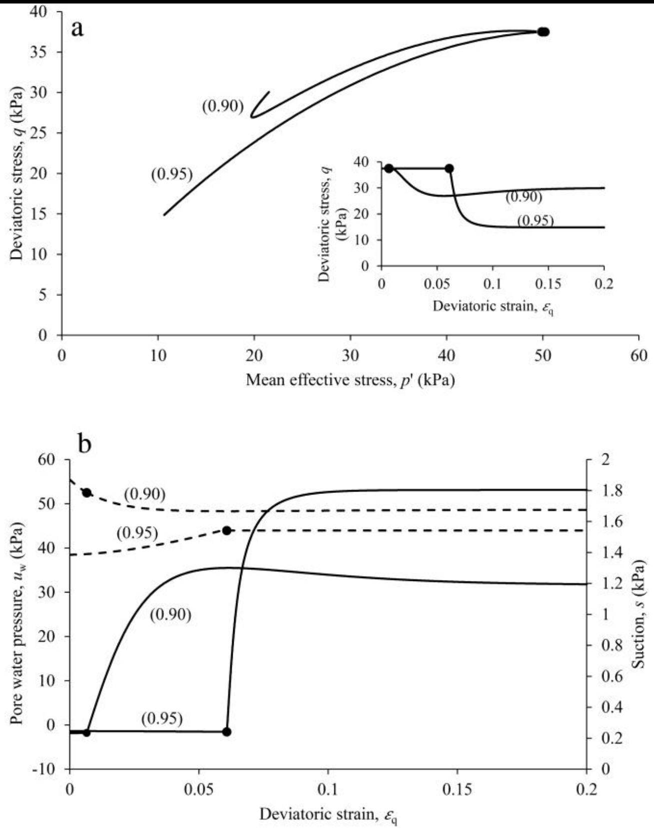
a
Deviatoric stress, q (kPa)
Mean effective stress, p' (kPa)
(0.90)
(0.95)
Deviatoric stress, q (kPa)
Deviatoric strain, ε_q
b
Pore water pressure, u_w (kPa)
Suction, s (kPa)
Deviatoric strain, ε_q

Figure 12

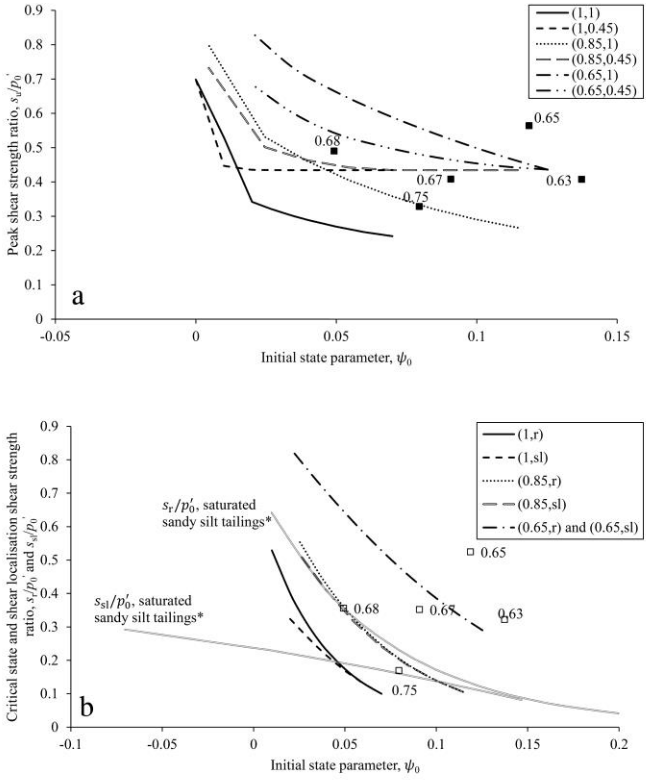
(1,1)
(1,0.45)
(0.85,1)
(0.85,0.45)
(0.65,1)
(0.65,0.45)
0.65
0.68
0.67
0.63
0.75
a
Peak shear strength ratio, s_u/p_0'
Initial state parameter, ψ_0
(1,r)
(1,sl)
(0.85,r)
(0.85,sl)
(0.65,r) and (0.65,sl)
s_r/p_0', saturated sandy silt tailings*
s_{sl}/p_0', saturated sandy silt tailings*
b
Critical state and shear localisation shear strength ratio, s_r/p_0' and s_{sl}/p_0'
Initial state parameter, ψ_0

Figure 13

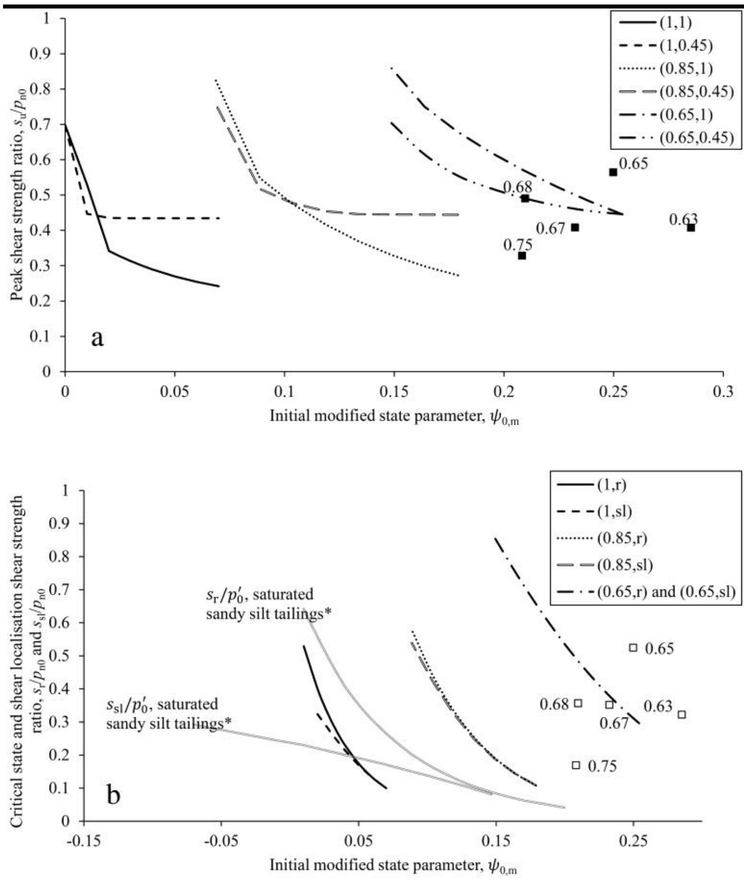
(1,1)
(1,0.45)
(0.85,1)
(0.85,0.45)
(0.65,1)
(0.65,0.45)
Peak shear strength ratio, s_u/p_{n0}
Initial modified state parameter, $\psi_{0,m}$
0.65
0.68
0.67
0.63
0.75
a
(1,r)
(1,sl)
(0.85,r)
(0.85,sl)
(0.65,r) and (0.65,sl)
s_r/p_0', saturated sandy silt tailings*
s_{sl}/p_0', saturated sandy silt tailings*
Critical state and shear localisation shear strength ratio, s_r/p_{n0} and s_{sl}/p_{n0}
b

Figure 14

Accepted manuscript doi:
10.1680/jgeot.22.00074

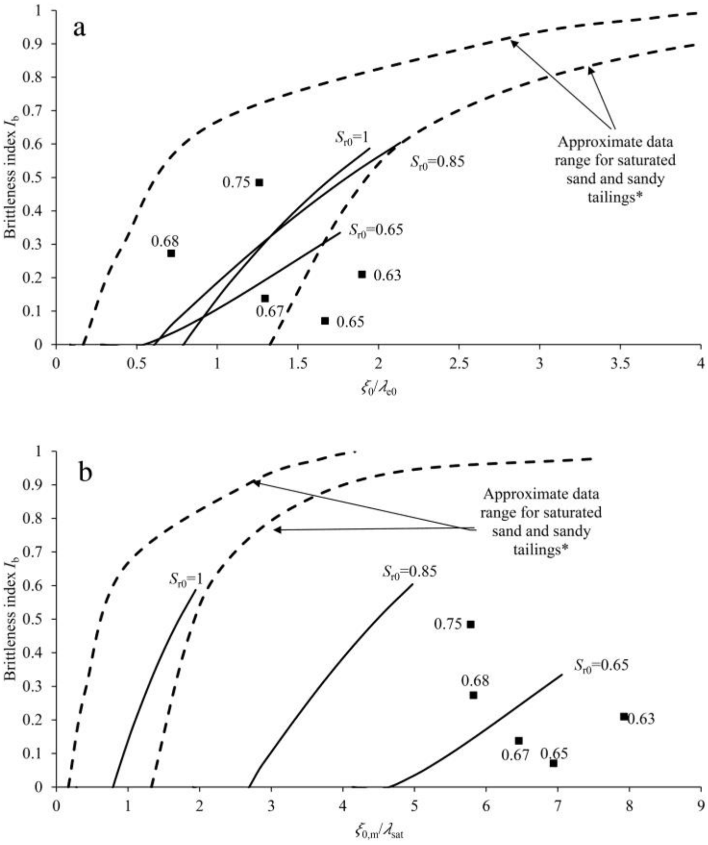

Figure 15